Supporting Information

Photonic spin-multiplexing metasurface for switchable spiral phase contrast imaging

Pengcheng Huo[1,2], Cheng Zhang[3,4], Wenqi Zhu[5,6], Mingze Liu[1], Song Zhang[1], Si Zhang[1], Lu Chen[5,6], Henri J. Lezec[5], Amit Agrawal[5,6], Yanqing Lu[1,2] and Ting Xu[1,2]

1. *National Laboratory of Solid-State Microstructures, Jiangsu Key Laboratory of Artificial Functional Materials, College of Engineering and Applied Sciences, Nanjing University, Nanjing 210093, China*
2. *Collaborative Innovation Center of Advanced Microstructures, Nanjing 210093, China*
3. *School of Optical and Electronic Information, Huazhong University of Science and Technology, Wuhan 430074, China.*
4. *Wuhan National Laboratory for Optoelectronics, Huazhong University of Science and Technology, Wuhan 430074, China.*
5. *Physical Measurement Laboratory, National Institute of Standards and Technology, Gaithersburg, Maryland 20899, United States*
6. *Maryland NanoCenter, University of Maryland, College Park, Maryland 20899, United States*

Supplementary Note 1: Phase contrast imaging using spiral phase masking function

In this work, $(u,\ v)$ and $(x,\ y)$ are the spatial coordinates at the metasurface (Fourier) and object (image) planes, respectively. (ρ,ϕ) and $(r,\ \varphi)$ are their polar coordinates that have the relation of $\begin{cases} \rho = \sqrt{u^2+v^2} \\ \phi = \arctan\,(v/u) \end{cases}$ and $\begin{cases} r = \sqrt{x^2+y^2} \\ \varphi = \arctan\,(y/x) \end{cases}$. Based on the imaging process of a 4f system, the output light field $E_{out}(x,y)$ of the object place and input light field $E_{in}(x,y)$ of the image plane can be associated by the spatial filter $M(\rho,\phi)$, and have the following relation,

$$E_{out}(x,y) = E_{in}(x,y)\otimes F\{M(\rho,\phi)\} = E_{in}(x,y)\otimes m(r,\ \varphi) \tag{S1}$$

Here, the symbol $\otimes$ represents convolution and $F\{\cdot\}$ denotes the Fourier transform of the masking function, $m(r,\ \varphi)$ is the point-spread function (PSF) that determines the filtering effect of the system and can be written as [1],

$$m(r,\varphi) = \frac{1}{i\lambda f}\int_0^{2\pi}\int_0^{\infty} M(\rho,\phi)\exp\left[-\frac{ik}{f}r\rho\cos\,(\phi-\varphi)\right]\rho d\rho d\phi \tag{S2}$$

where $k = 2\pi/\lambda$ is the light wave vector, f is the focal length of the lens. Considering a spiral phase mask filter of a circular aperture with radius R,

$$M_2(\rho,\phi) = exp\ (i\phi) \tag{S3}$$

According to Eq. (S2), the PSF of the filter can finally be expressed as,

$$m_2(r,\varphi) = -\frac{k}{f}\exp\,(i\varphi)\int_0^R J_1(\frac{kr\rho}{f})\rho d\rho \tag{S4}$$

Combined with the recurrence relation of the Bessel function [2, 3], it can be deduced as follows,

$$m_2(r,\varphi) = -\frac{\pi R}{2r}[J_1(\tau)H_0(\tau) - J_0(\tau)H_1(\tau)]\exp\,(i\varphi) \tag{S5}$$

where $\tau = kRr/f$. J_0 and J_1 are Bessel functions of zero and first order, respectively. H_0 and H_1 are Struve functions of zero and first order, respectively. The PSF (m_2) can be regarded as the formation of a vortex that has a doughnut shaped intensity distribution and a spiral phase profile changing from 0 to 2π for one turn. Then the output field obtained at the object plane of 4f system is written as,

$$E_{out}(x,y) = E_{in}(x,y)\otimes m_2(r,\varphi) = -E_{in}(x,y)\otimes\frac{\pi R}{2r}[J_1(\tau)H_0(\tau) - J_0(\tau)H_1(\tau)]\exp\,(i\varphi) \tag{S6}$$

In the convolution process of Eq. (S6), the $m_2(r,\varphi)$ with vortex element will be weighted to superimpose on each point of input light field $E_{in}(x,y)$, and then integrated over the whole area to determine the amplitude of the corresponding point of output light field $E_{out}(x,y)$. Due to the phase difference of π in the opposite azimuth of the vortex element, integrating the uniform area of E_{in} will lead to destructive interference and a dark background. In contrast, arbitrarily unevenness in the region of integration including amplitude gradient and phase gradient will remove the destructive interference and result in bright regions. On the other hand, assuming incident field $E_{in}(x,y) = |E_{in}|\exp(i\psi_{in})$, the spiral phase filtering properties also can be quantified by Taylor expanding E_{in} and solving Eq. (S6) [4],

$$E_{out} \propto \exp(i\psi_{in}) G_A \exp(i\delta_A) + iE_{in} G_P exp(i\delta_P) \tag{S7}$$

where G_A and G_P (δ_A and δ_P) are the magnitudes (phase) of the gradients of the input field amplitude and the input filed phase, respectively:

$$\boldsymbol{G_A} = \nabla |E_{in}| = G_A exp(i\delta_A)\boldsymbol{e_A} \tag{S8}$$

$$\boldsymbol{G_P} = \nabla |\psi_{in}| = G_P exp(i\delta_P)\boldsymbol{e_P} \tag{S9}$$

The output field of Eq. (S7) consists of two terms that describe the effects of amplitude and phase variations of the input field in spiral phase filtering. The two terms are proportional to the absolute values of the gradients $\boldsymbol{G_A}$ and $\boldsymbol{G_P}$ respectively, which results in strong isotropic enhancement of amplitude and phase edge. In additional, combining with the analytical result of eq. (S7), it shows that the spiral phase filtering operation is equivalent to the two-dimensional spatial differentiation of incident light field in principle. The corresponding spatial spectral transfer function can be calculated by the relation of $H(k_x, k_y) = E_{out}(u,v)/E_{in}(u,v)$ and shown in Fig. S1.

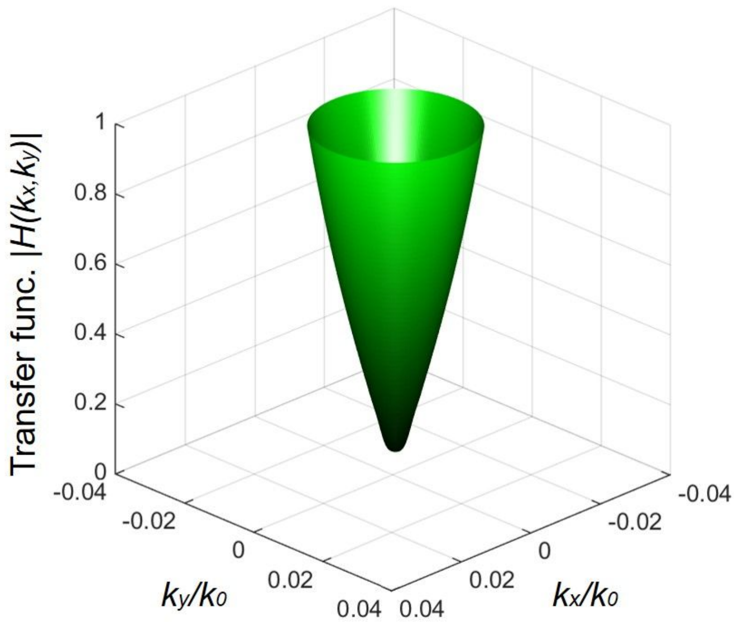

Figure S1. The calculated spatial spectral transfer function of the spiral phase filtering operation.

Supplementary Note 2: Derivation of the Jones matrix J and its eigenvalues and eigenvectors.

Assuming light incident upon the planar optical metasurface filter is in two orthogonal spin states $|L\rangle = \frac{1}{\sqrt{2}}\begin{bmatrix}1\\ i\end{bmatrix}$ and $|R\rangle = \frac{1}{\sqrt{2}}\begin{bmatrix}1\\ -i\end{bmatrix}$, where $|L\rangle$ and $|R\rangle$ denote left- and right-circular polarization (LCP and RCP) in the linear polarization basis. In order to independently implement two different masking function ($M_1(\rho,\phi) = exp\ (ic_0)$ and $M_2(\rho,\phi) = exp\ (i\phi)$, with c_0 being a constant) for the incident plane wave propagating along the *z*-direction respectively in LCP and RCP states, the optical metasurface should be described by a Jones matrix *J* that simultaneously satisfies,

$$J(\rho,\phi)|L\rangle = M_1(\rho,\phi)|R\rangle \tag{S10}$$

and

$$J(\rho,\phi)|R\rangle = M_2(\rho,\phi)|L\rangle \tag{S11}$$

Upon matrix inversion of Eq. (S10) and (S11) we obtain the form as

$$J(\rho,\phi) = \begin{bmatrix} M_1 & M_2 \\ -iM_1 & iM_2 \end{bmatrix}\begin{bmatrix} 1 & 1 \\ i & -i \end{bmatrix}^{-1} \tag{S12}$$

Then, we can show that the desired matrix J is

$$J(\rho,\phi) = \frac{1}{2}\begin{bmatrix} (M_1 + M_2) & -i(M_1 - M_2) \\ -i(M_1 - M_2) & -(M_1 + M_2) \end{bmatrix} \tag{S13}$$

The unitary of this matrix guarantees that it can be decomposed into the following form $J = \gamma\Delta\gamma^{-1}$, where γ is a real unitary matrix whose columns are the eigenvectors of J, and Δ is a diagonal matrix whose elements are the eigenvalues of J. By solving the characteristic equation of the Jones matrix J, we can find its eigenvalues as,

$$\xi_1 = e^{i[\frac{1}{2}(c_0 + \phi)]} \qquad \xi_2 = e^{i[\frac{1}{2}(c_0 + \phi) - \pi]} \tag{S14}$$

and eigenvectors as

$$|\lambda_1\rangle = \begin{bmatrix} \cos\frac{1}{4}(c_0 - \phi) \\ sin\frac{1}{4}(c_0 - \phi) \end{bmatrix} \qquad |\lambda_2\rangle = \begin{bmatrix} -\sin\frac{1}{4}(c_0 - \phi) \\ cos\frac{1}{4}(c_0 - \phi) \end{bmatrix} \tag{S15}$$

Thus, the Jones matrix can be decomposed into the following form,

$$J(\rho,\phi) = \gamma\Delta\gamma^{-1} = \begin{bmatrix} \cos\frac{1}{4}(c_0 - \phi) & -\sin\frac{1}{4}(c_0 - \phi) \\ sin\frac{1}{4}(c_0 - \phi) & cos\frac{1}{4}(c_0 - \phi) \end{bmatrix}\begin{bmatrix} e^{i[\frac{1}{2}(c_0 + \phi)]} & 0 \\ 0 & e^{i[\frac{1}{2}(c_0 + \phi) - \pi]} \end{bmatrix}$$
$$\begin{bmatrix} \cos\frac{1}{4}(c_0 - \phi) & \sin\frac{1}{4}(c_0 - \phi) \\ -sin\frac{1}{4}(c_0 - \phi) & cos\frac{1}{4}(c_0 - \phi) \end{bmatrix} \tag{S16}$$

Since Jones matrix J works in the linear polarization basis and γ can be regarded as a rotation matrix for the matrix Δ, In contrast to a normal linear birefringent wave-plate rotated through some angle θ, the values of phase shifts φ_x and φ_y along the two symmetry axes and θ all depend on the spatial coordinate, and can be written as the analytical expression,

$$\varphi_x = \frac{1}{2}(c_0 + \phi) \tag{S17}$$

$$\varphi_y = \frac{1}{2}(c_0 + \phi) - \pi \tag{S18}$$

$$\theta = \frac{1}{4}(c_0 - \phi) \tag{S19}$$

The phase difference π between φ_x and φ_y requires the element structure of the metasurface to act as a half wave plate (HWP). Based on the Eq. (S17) - (S19), the dependence of phase shifts (φ_x, φ_y) and the rotation angle θ of the HWPs on the spatial coordinates in the metasurface device are calculated and shown in Fig. S1.

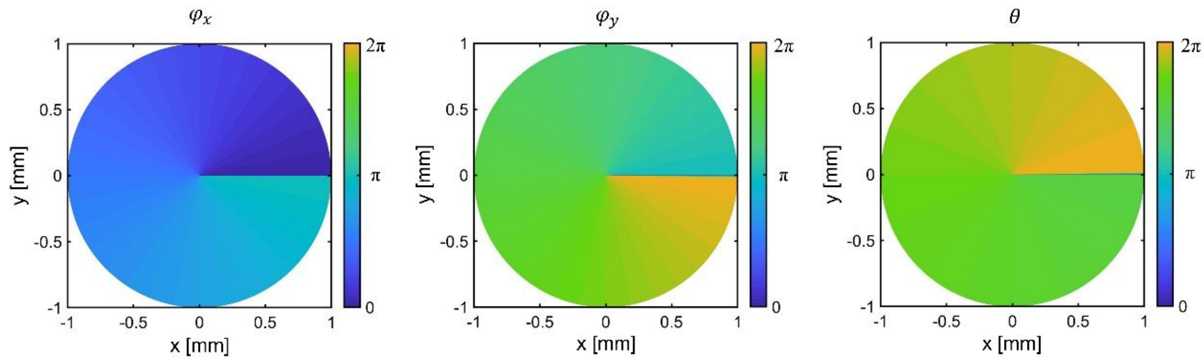

Figure S2. Calculated phase shifts φ_x and φ_y along the two symmetry axes of HWPs and the rotational angle θ as a function of the spatial coordinate with $C_0 = 0$.

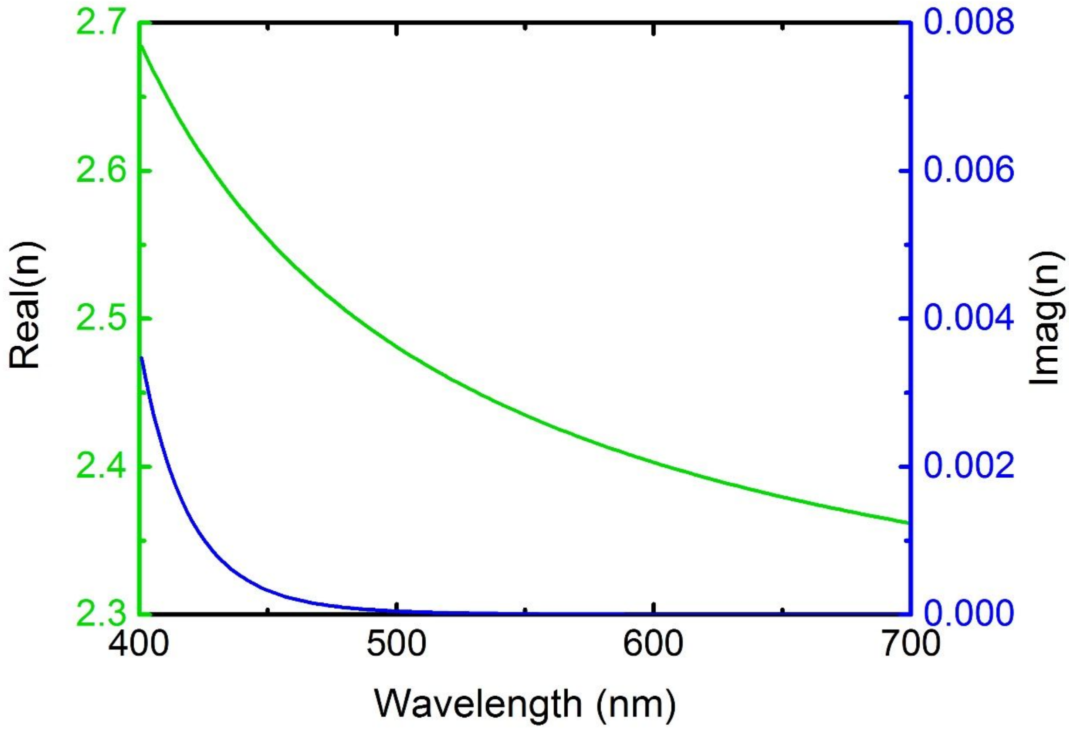

Figure S3. Refractive index of atomic layer deposition (ALD) TiO_2. The real and imaginary part of the refractive index (*n*) of 64 nm thick ALD TiO_2 is measured using spectroscopic ellipsometry.

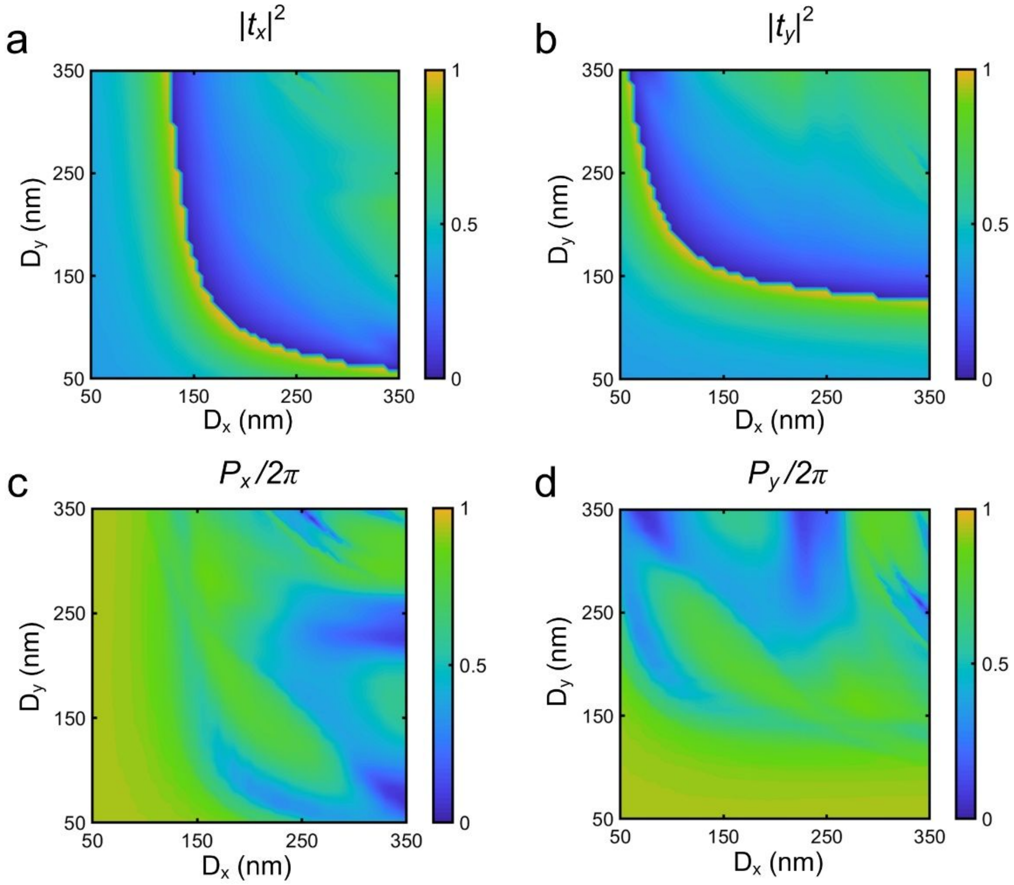

Figure S4. Simulated normalized intensity transmission coefficients and phase shifts as a function of rectangular nanopillar dimensions at the wavelength of 530 nm. Intensity transmission coefficients ($|t_x|^2$and$|t_y|^2$) and the phase (P_x and P_y) of x and y-polarized optical waves for the periodic array of TiO_2 rectangular nanopillars with $\theta = 0$. Each point in the spectra map corresponds to a nanopillar with a specific (D_x, D_y) combination.

Supplementary Note 3: Effect of the segment number of spiral phase on imaging

The perfect masking function $M_2(\rho,\phi)$ presented in eq. (S3) has a continuous and smooth phase. In fact, the one imparted on the metasurface filter is discretized and can be written as,

$$M_2(\rho,\phi) = exp\ (i\text{fix}(\frac{n\phi}{2\pi})\frac{2\pi}{s}) \tag{S20}$$

where $(\rho,\ \phi)$ is the polar coordinate, s denotes the segment number of masking function M_2 imparted on the metasurface filter. fix(X) can round the elements of X to the nearest integers towards zero. In Fig. S5, we calculate the phase contrast imaging using the spiral phase function with segment number of 1, 4, 8, 16, respectively. They show that the imaging results gradually approach the perfect spiral phase contrast imaging with the increase of the segment number. On the other hand, in order to quantify the effect of segment number (s) in spiral phase on imaging quality and obtain the proper degree of discretization of HWPs in the full range [0, 2π], the mean square error (*MSE*) function has been adopted as,

$$MSE(s) = \frac{\sum_{a\ =1}^{A}\sum_{b\ =1}^{B}|I(a\ ,b) - I_s(a\ ,b\ )|^2}{A\ \times B} \tag{S21}$$

where $I(a,b)$ and $I_s(a,b)$ represent the imaging results by adopting a perfect and the s-segment spiral phase filter, respectively. A and B are the sampling number of the image in plane dimension. The *MSE* curve between the imaging results obtained using a perfect spiral phase and the spiral phase with different step numbers is calculated and shown in Fig. S6. The *MSE* has been reduced to a negligible value with the segment number s≥16. After a comprehensive analysis of imaging quality and design difficulty, s = 16 is selected as the segment number of masking function.

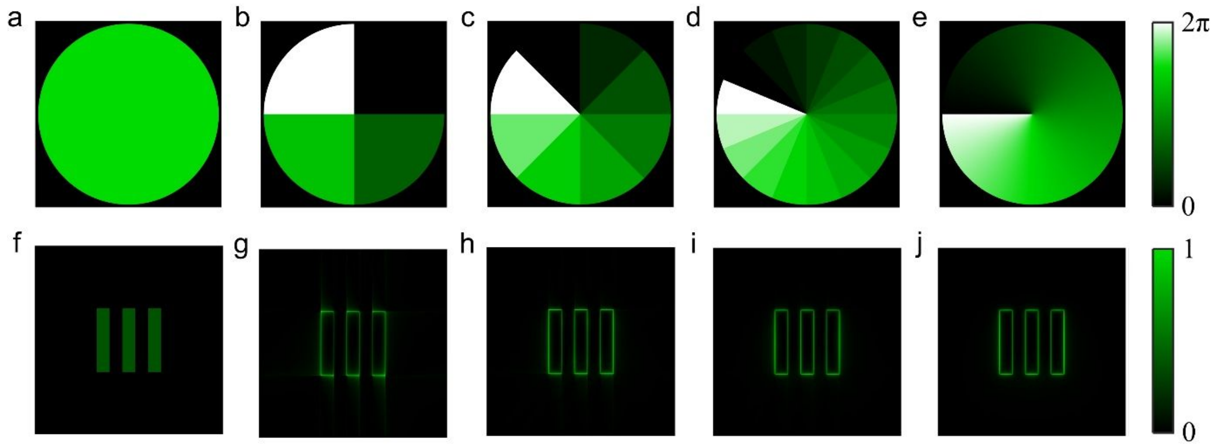

Figure S5. Calculated phase contrast imaging using the spiral phase filter with different segment number. a-d, show the phase distribution of the spiral phase filter with the segment number of 1, 4, 8, 16, respectively. **e**, The phase distribution of a perfect spiral filter. **f-j**, The corresponding imaging results. The imaging results gradually approach the perfect spiral phase contrast imaging with the increase of the segment number.

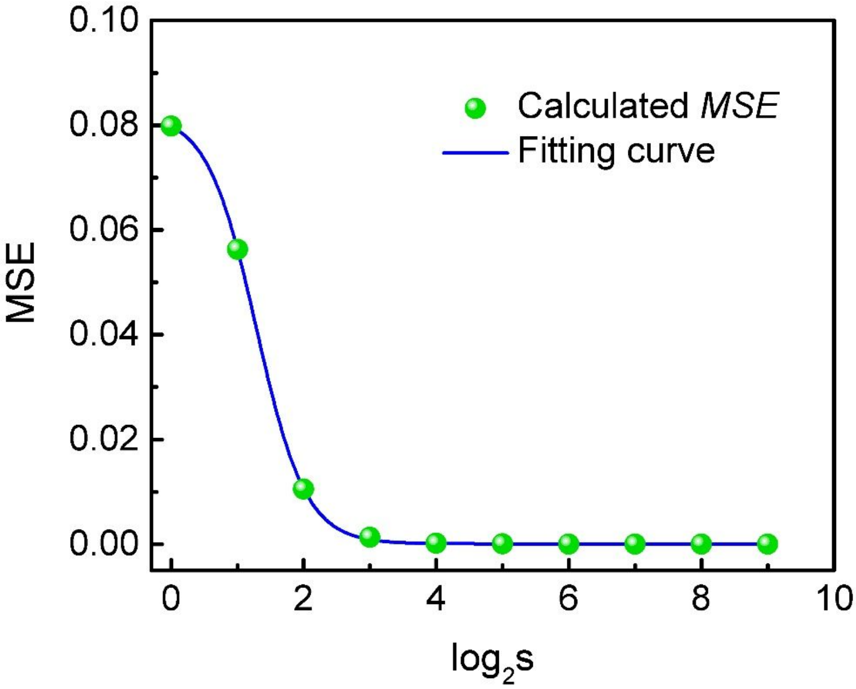

Figure S6. Calculated mean square error function (MSE) curve between the imaging results obtained using a perfect spiral phase and the spiral phase with different step numbers. The curve can be used to quantify the effect of steps number (*s*) in spiral phase on imaging quality and determine the degree of discretization of HWPs in the full range [0, 2π].

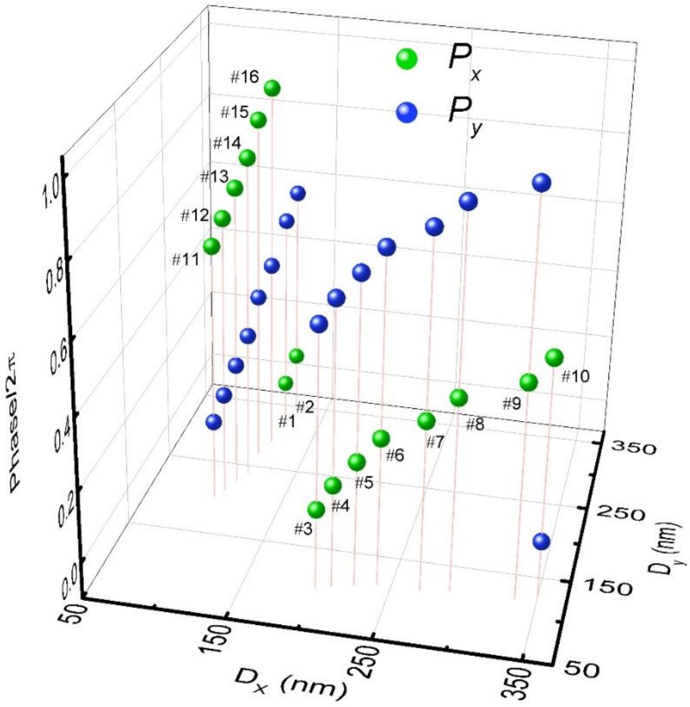

Figure S7. The dimension distribution and phase shifts of the chosen TiO_2 rectangular nanopillars at the wavelength of 530 nm. Green and blue spheres mark the phase shifts (P_x and P_y,) of the chosen 16-level nanopillars. Each level corresponds to a specific TiO_2 nanopillar HWP. The structural parameters of the nanopillars are optimized so that the transmission coefficients and polarization conversion efficiencies are high enough across the full visible region.

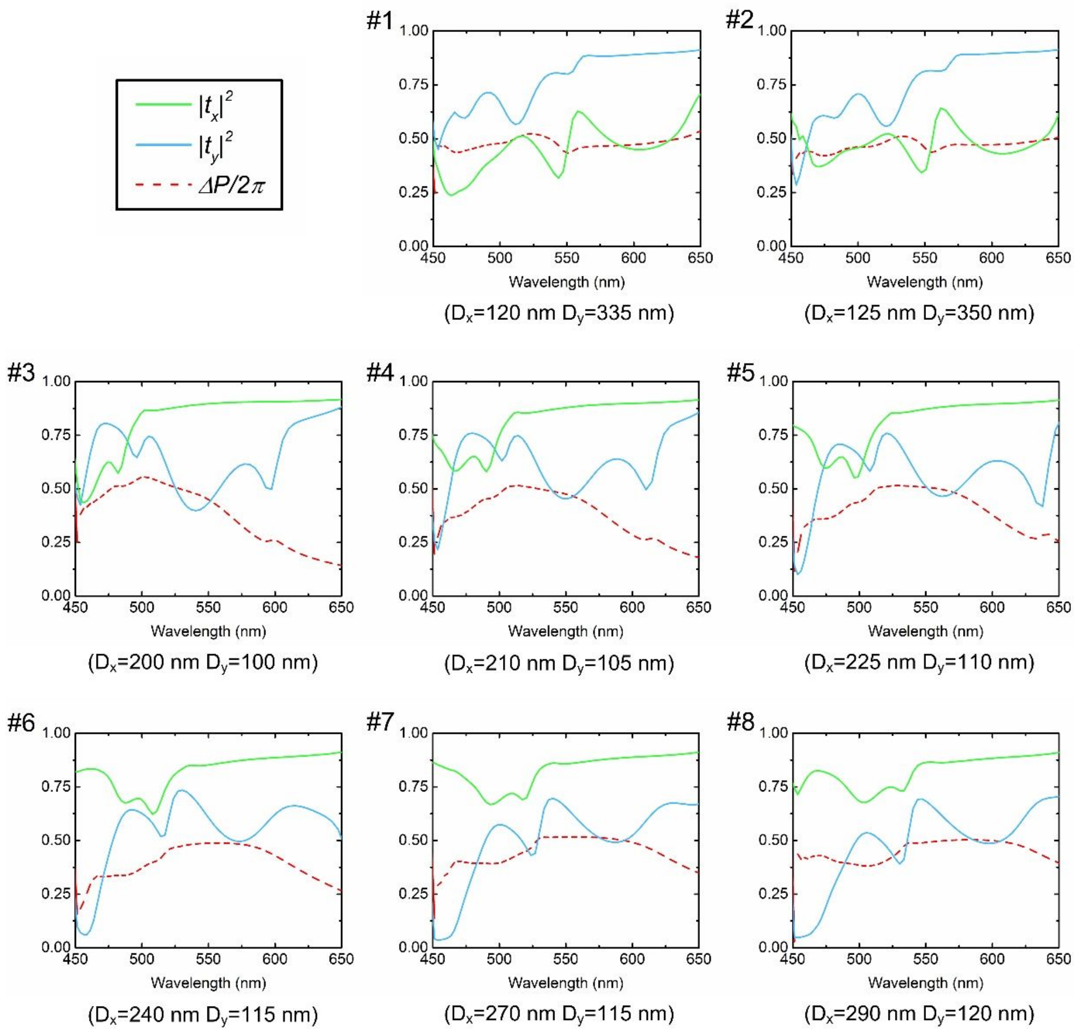

Figure S8. Wavelength dependence of the intensity transmission coefficients ($|t_x|^2$ and $|t_y|^2$) and the phase difference ($\Delta P = P_x - P_y$) of x and y-polarized optical waves for periodic arrays of selected nanopillars. The spectra are shown for eight nanopillars with different (D_x, D_y) combination: #1 (120 nm, 335 nm), #2 (125 nm, 350 nm), #3 (200 nm, 100 nm), #4 (210 nm, 105 nm), #5 (225 nm, 110 nm), #6 (240 nm, 115 nm), #7 (270 nm, 115 nm), #8 (290 nm, 120 nm). The transmission and phase spectra for the remaining eight nanopillars can be obtained by swapping x and y in the spectra graphs.

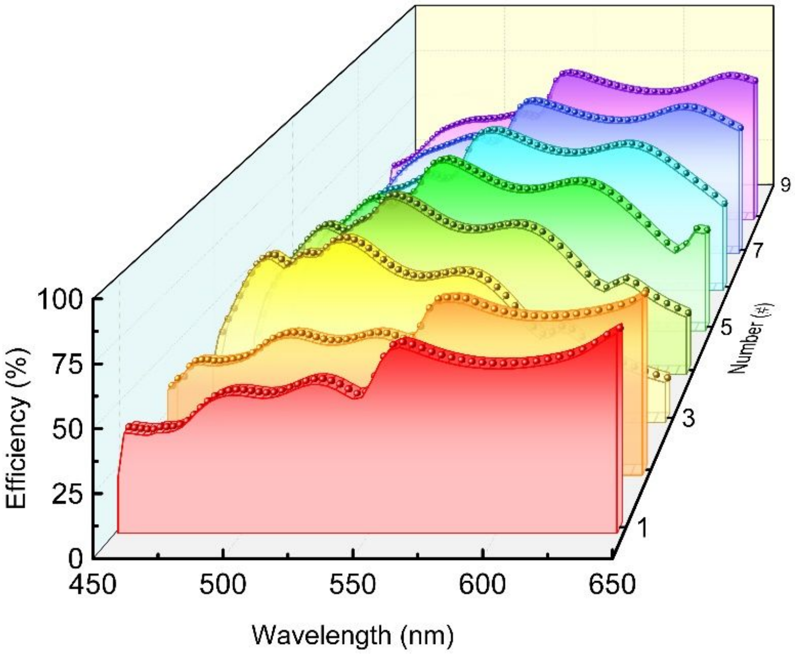

Figure S9. Calculated polarization conversion efficiency for the selected eight rectangular nanopillars in the entire visible range. The structural parameters of the nanopillars are optimized so that the transmission coefficients and polarization conversion efficiencies for the incident light are high enough across the full visible region. The remaining eight rectangular nanopillars have the same polarization conversion efficiency as the ones given in the spectra.

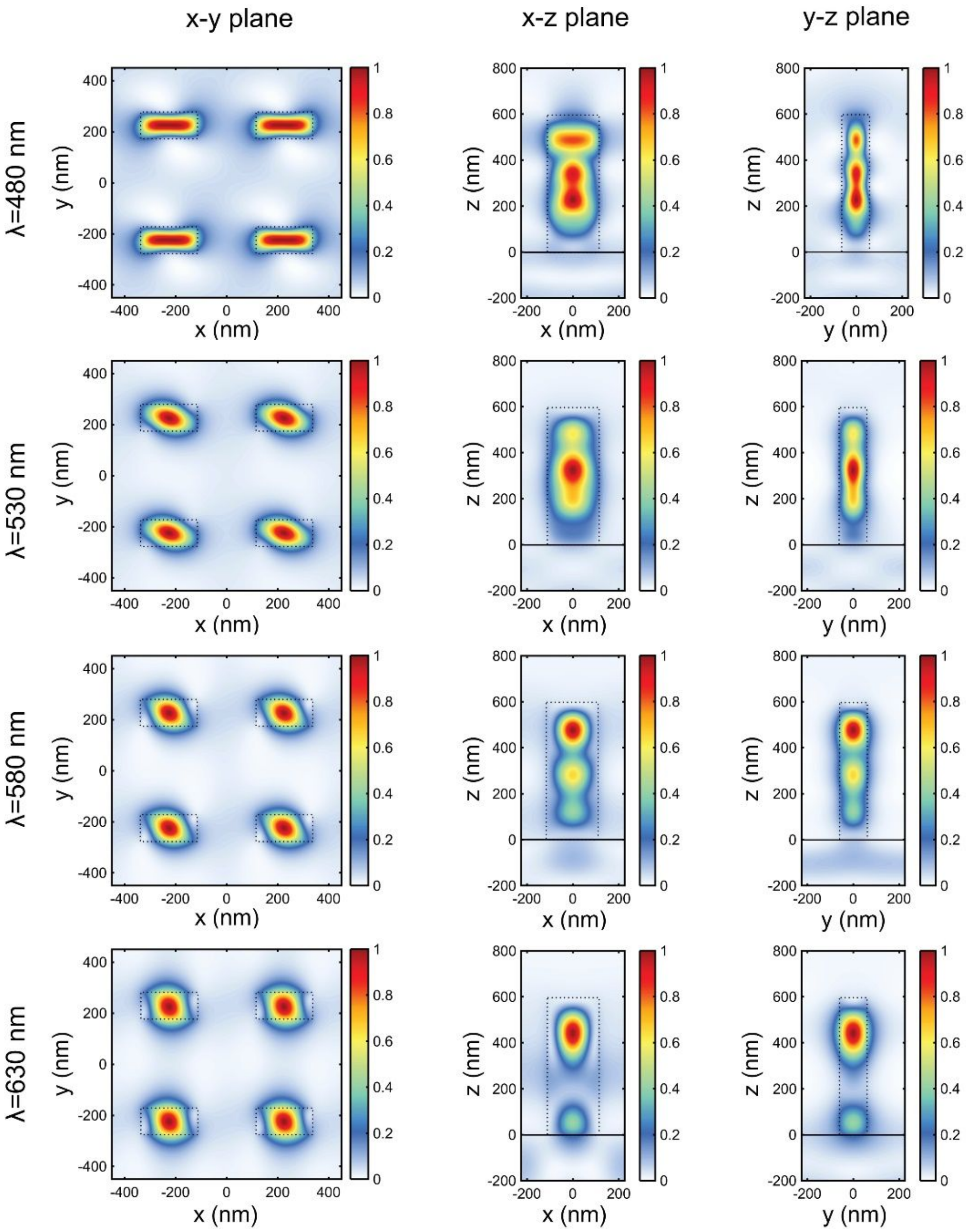

Figure S10. The normalized magnetic energy density distribution of the nanopillars periodic arrays for LCP plane wave illumination at the wavelength of 480 nm, 530 nm, 580 nm, and 630 nm, respectively. Top views (left: *x-y* plane) and side views (middle: *x-z* plane and right: *y-z* plane). The results show that the normalized magnetic energy density is mainly confined inside the TiO_2 nanopillar. The coupling effect between neighboring nanopillars is very weak.

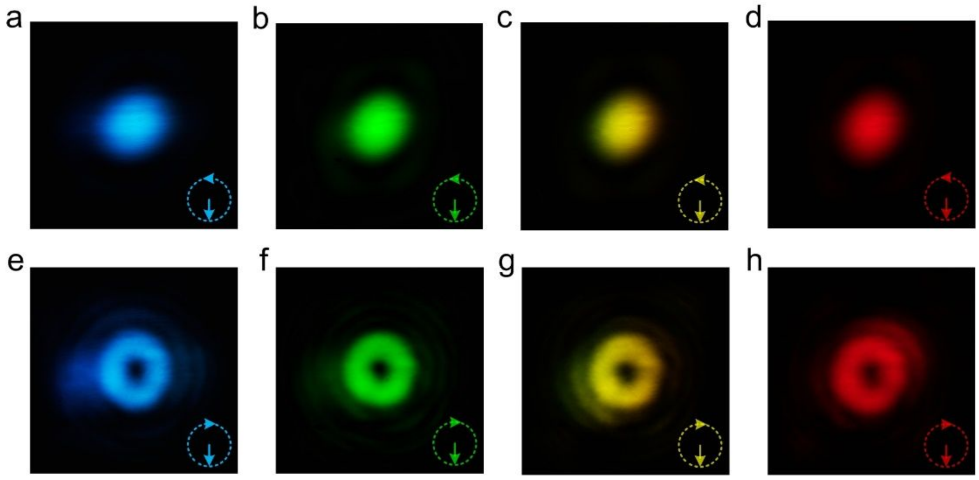

Figure S11. Measured intensity distributions of output states for LCP and RCP incident light illumination at the wavelength of 480 nm, 530 nm, 580 nm, and 630 nm. a-d, show a Gaussian distribution for LCP incident light and **e-h**, show the donut intensity distribution for RCP incident light, which demonstrate that the spin-dependent metasurface spatial filter is able to implement two independent masking functions in the entire visible frequency.

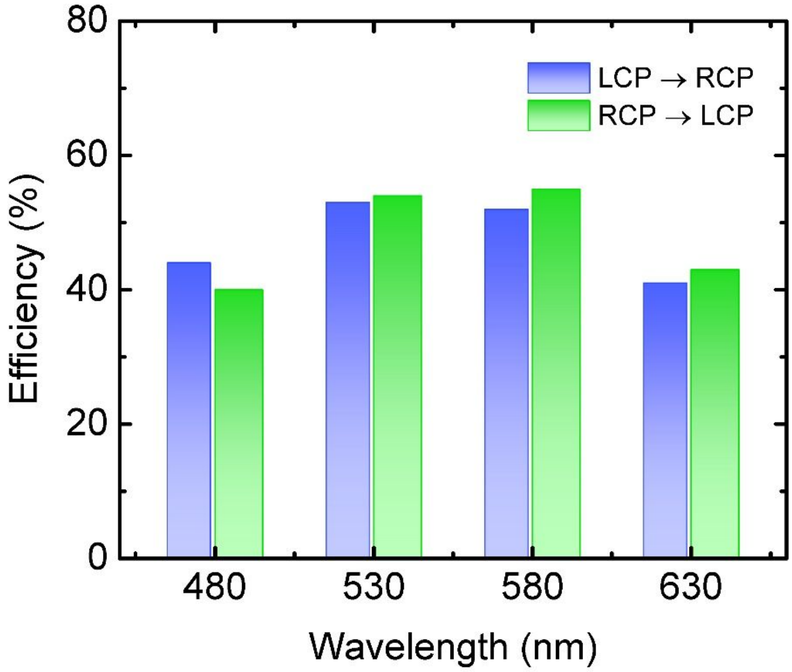

Figure S12. The measured conversion efficiency of the metasurface device for LCP and RCP incident light illumination at the wavelength of 480 nm, 530 nm, 580 nm, and 630 nm, respectively. The high conversion efficiency is mainly due to low-loss material selection of TiO_2 and parameters optimization of HWPs-nanopillars.

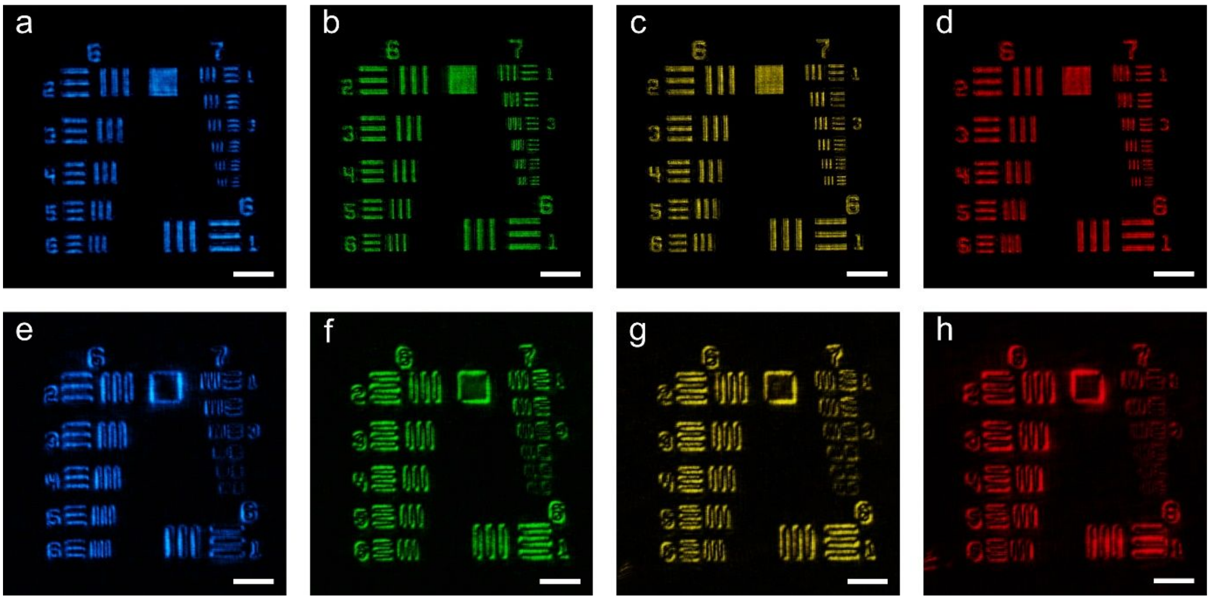

Figure S13. Investigation of the system resolution for two imaging modes in the visible region. a-d, the bright-field imaging mode at the wavelength of 480 nm, 530 nm, 580 nm, and 630 nm, respectively, the smallest line pair that can be resolved in the resolution test chart is elements 6 of group 7 (228 lp/mm), which corresponds a resolution of 2.19 µm along the x and y direction. **e-f**, for phase contrast imaging mode, the smallest line pair that can be resolved in the resolution test chart is elements 3 of group 7 (161 lp/mm), which corresponds to a resolution of 3.11 µm. Scale bar: 50 µm.

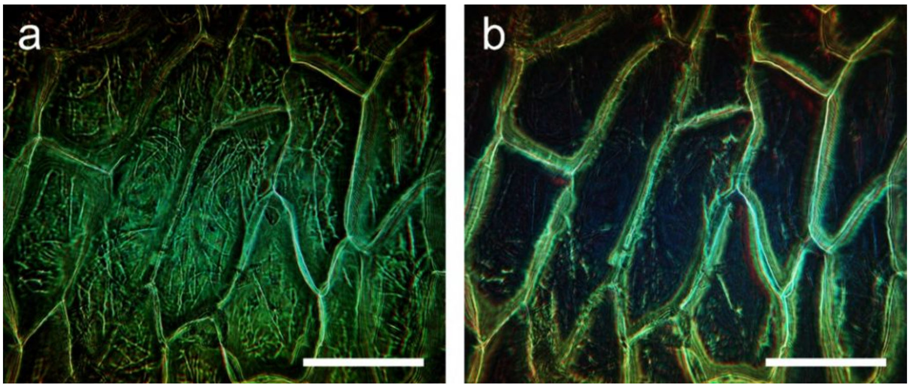

Figure S14. The bright-field and edge-enhanced phase contrast images of the undyed onion epidermal cells illuminated by a white light beam. Images are captured with a 20 × objective lens. a, Traditional bright-field images for LCP plane wave illumination. **b**, Edge-enhanced phase contrast images for RCP plane wave illumination. Scale bar: 100 μm.

Supplementary Reference

[1] G. O. Reynolds, J. B. Develis, and B. J. Thompson, *The New Physical Optics Notebook: Tutorials in Fourier Optics* (SPIE, 1989).

[2] M. Abramowitz and I. A. Stegun, *Handbook of Mathematical Functions with Formulas, Graphs, and Mathematical Tables* (Dover, 1970).

[3] S. N. Khonina, V. V. Kotlyar, M. V. Shinkaryev, V. A. Soifer, and G. V. Uspleniev, The phase rotor filter, *J. Mod. Opt.* **39**, 1147–1154 (1992).

[4] A. Jesacher, S. Furhapter, S. Bernet, and M. Ritsch-Marte, Spiral interferogram analysis, *J. Opt. Soc. Am. A* **23**, 1400-1409 (2006).